Nanoscale

ROYAL SOCIETY OF CHEMISTRY

PAPER

View Article Online
View Journal | View Issue

Check for updates

Cite this: *Nanoscale*, 2022, **14**, 18010

A study on the role of plasmonic $Ti_3C_2T_x$ MXene in enhancing photoredox catalysis†

Guanshun Xie,[a] Chuang Han,[b] Fei Song,[a] Yisong Zhu,[a] Xuanyu Wang,[a] Jialin Wang,[a] Zhenjun Wu,[c] Xiuqiang Xie *[a] and Nan Zhang [a]

Received 26th October 2022,
Accepted 9th November 2022

DOI: 10.1039/d2nr05983e

rsc.li/nanoscale

Engineering the spatial separation and transfer of photogenerated charge carriers has been one of the most enduring research topics in the field of photocatalysis due to its crucial role in determining the performances of photocatalysts. Herein, as a proof-of-concept, $Ti_3C_2T_x$ MXene is coupled with a typical heterojunction of TiO_2@CdS through a co-assembly strategy to boost electron pumping towards improving the photocatalytic efficiency. In addition to the band alignment-mediated electron transfer in TiO_2@CdS–$Ti_3C_2T_x$ heterojunctions, the plasmon-induced electric field enhancement of $Ti_3C_2T_x$ is found to cooperate with the electron-reservoir role of $Ti_3C_2T_x$ to extract photoinduced electrons. The synergistic dual functions of $Ti_3C_2T_x$ promote multichannel electron transfer in TiO_2@CdS–$Ti_3C_2T_x$ hybrids to improve the photocatalytic efficiency. These results intuitively show that there is a wide scope to manipulate the spatial separation and transfer of photoinduced electrons by cultivating the fertile ground of $Ti_3C_2T_x$ toward boosting the efficiency of solar-to-chemical conversion.

Published on 19 1401. Downloaded on 08/11/1404 05:47:49 ..

1. Introduction

Photoredox catalysis holds great promise as an alternative to traditional synthetic pathways and is an ideal strategy to solve the growing global energy crisis.[1–3] The bulk recombination of photoinduced charge carriers has been a long-standing challenge fundamentally restricting the solar-to-chemical conversion efficiency over photocatalysts.[4–8] Under this background, engineering appropriate cocatalysts to steer photo-induced electron transfer has been an enduring research theme.[9–15]

MXene is a large family of two-dimensional (2D) transition metal carbides, nitrides, and carbonitrides with the general formula of $M_{n+1}X_nT_x$ (n = 1, 2, or 3), where M is an early transition metal, X represents carbon and/or nitrogen, and T_x represents surface functionalities (such as –OH, –O and/or –F).[16,17] Since $Ti_3C_2T_x$ MXene has been prepared successfully for the first time in 2011,[18] its chemical and structural versatility, such as a 2D lamellar structure with exposed metastable transition metals, hydrophilicity, and high electrical conductivity,[19] endows $Ti_3C_2T_x$ with great promise in the field of photocatalysis.[20–23] Thus far, enormous endeavors have been predominantly focused on using $Ti_3C_2T_x$ to construct single electron transfer channels based on the Schottky effect to improve the charge carrier separation efficiency toward boosting the photocatalytic performance.[24–26] Very recently, metallic $Ti_3C_2T_x$ MXene has been found to exhibit the attracting localized surface plasmon resonance (LSPR) effect,[27–30] which results from its high carrier density (~8×10^{21} cm^{-3})[31] and strong absorption of electromagnetic waves.[32] The strong electron–phonon collision in $Ti_3C_2T_x$ with a large absorption cross-section and an ultrathin-atomic-layer structure enables efficient light absorption across a wide spectrum in the visible-near-infrared (NIR) region,[33–36] which is not valid for other

[a]College of Materials Science and Engineering, Hunan University, Changsha 410082, P. R. China. E-mail: xiuqiang_xie@hnu.edu.cn
[b]Department of Chemistry, University of Cincinnati, USA
[c]College of Chemistry and Chemical Engineering, Hunan University, P. R. China
†Electronic supplementary information (ESI) available. See DOI: https://doi.org/10.1039/d2nr05983e

Xiuqiang Xie

Dr Xiuqiang Xie is now an associate professor in the College of Materials Science and Engineering, Hunan University. He received his PhD degree from the University of Technology Sydney in 2017 under the supervision of Prof. Guoxiu Wang. He has been a visiting PhD student supervised by Prof. Yury Gogotsi at Drexel University, where he started his research on MXenes. His current research interests include the optical properties and the assembly methods of MXenes for sustainable technologies, such as photocatalysis and hybrid alkali-ion capacitors.

This journal is © The Royal Society of Chemistry 2022

Published on 19 1401. Downloaded on 08/11/1404 05:47:49 ..

two-dimensional materials, such as reduced graphene oxide (RGO). Compared to traditional plasmonic metals,[37–39] $Ti_3C_2T_x$ generates hot carriers with a rather slow relaxation due to a longer electronic free mean path.[36] Furthermore, in addition to modulating the geometrical features, it is also possible to tune the LSPR effect of $Ti_3C_2T_x$ by controlling the population of T_x moieties compatible with most polar semiconductor photocatalysts,[40–43] which is not possible for classical plasmonic metals. These merits underline the possibilities of using $Ti_3C_2T_x$ as a cocatalyst to enhance the photocatalytic performance of semiconductors by taking advantage of the potential LSPR effect, which, however, has been rarely explored.

Herein, as a proof-of-concept, we report on the application of $Ti_3C_2T_x$ to enhance the charge carrier separation of TiO_2@CdS as a typical heterojunction photocatalyst. Specifically, CdS is photodeposited on the surface of TiO_2 nanosheets to construct the typical heterojunction of TiO_2@CdS. $Ti_3C_2T_x$ MXene is then coupled with TiO_2@CdS *via* an electrostatic self-assembly approach. It is found that the introduction of $Ti_3C_2T_x$ MXene not only serves as an "electron reservoir" resulting from the Schottky junction effect, but also enhances the near electric field due to the LSPR effect. The dual functions of $Ti_3C_2T_x$ MXene synergized with the band-alignment mediated electron transfer in TiO_2@CdS afford multichannel electron transfer in the ternary TiO_2@CdS–$Ti_3C_2T_x$ hybrids. This results in the enhancement of the solar-to-chemical conversion efficiency compared to the traditional TiO_2@CdS binary composite.

2. Results and discussion

The schematic illustration for the preparation of TiO_2@CdS–$Ti_3C_2T_x$ composite photocatalysts is shown in Fig. 1a, in which CdS is photodeposited on the surface of TiO_2 nanosheets to construct the typical heterojunction of TiO_2@CdS. Then $Ti_3C_2T_x$ MXene is coupled with TiO_2@CdS *via* an electrostatic self-assembly approach. Typically, CdS is photodeposited on ultra-thin 2D TiO_2 nanosheets to generate TiO_2@CdS (TC) binary heterostructures. By increasing the feedstock of TiO_2

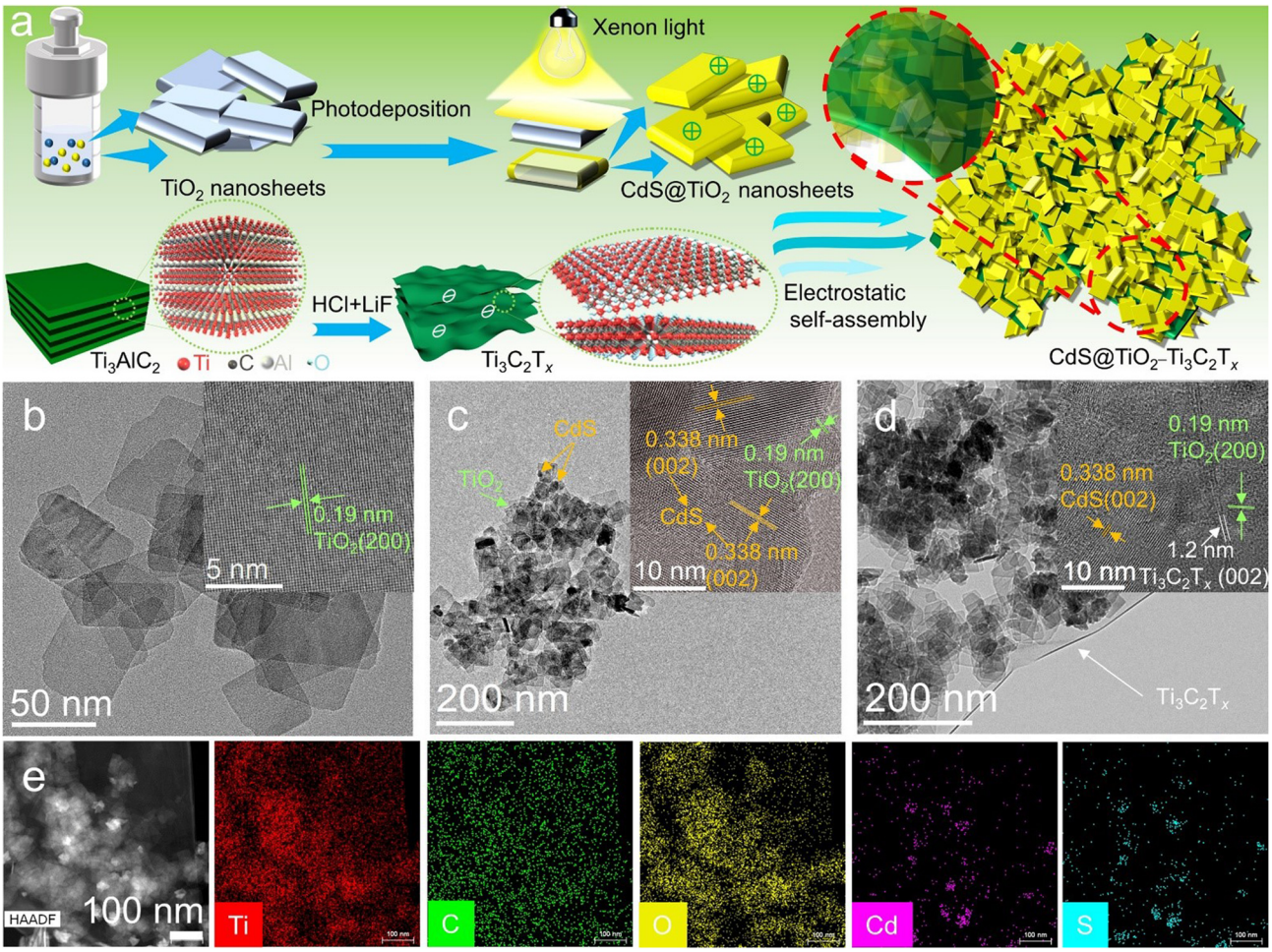

Fig. 1 Fabrication of TC-MX ternary heterostructures. (a) Schematic illustration for the preparation of TC-MX ternary heterostructures. The morphologies and textural structures of the samples. TEM images of (b) TiO_2, (c) TC-2 and (d) TC-0.1MX; the insets are the corresponding HRTEM images. (e) HAADF-STEM image of TC-0.1MX with the corresponding Ti, C, O, Cd, and S EDX mapping results.

Published on 19 1401. Downloaded on 08/11/1404 05:47:49 ..

while keeping the photodeposition of CdS unchanged, TiO_2@CdS composites with different TiO_2/CdS ratios (denoted as TC-1, TC-2, and TC-3) have been prepared. The zeta potentials of TC-1, TC-2, and TC-3 are calculated to be 25, 20, and 15 mV, respectively (Fig. S1a†), while $Ti_3C_2T_x$ is negatively charged with a zeta potential of −41 mV (Fig. S1b†). Therefore, the electrostatic interactions between TC and $Ti_3C_2T_x$ enable the construction of TiO_2@CdS–$Ti_3C_2T_x$ composites. The zeta potential of TC-MX increases positively with the increase of the $Ti_3C_2T_x$ amount due to the neutralization of the surface charge (Fig. S1c†). The resulting composites are labelled as TC-0.1MX, TC-0.2MX, and TC-1.0MX, corresponding to TC-MX samples with $Ti_3C_2T_x$ weight ratios of 0.1%, 0.2%, and 1.0%, respectively.

The crystal phase structures of the samples have been investigated by X-ray diffraction (XRD). As shown in Fig. S2,† it is clear that pure TiO_2, TC, and TC-MX composites all feature the characteristic diffraction peaks of anatase TiO_2 (JCPDS no. 73-1764),[44] and the characteristic diffraction peaks of hexagonal CdS (JCPDS no. 80-0006)[45] are observed for TC and TC-MX composites, indicating that CdS has been successfully photodeposited on the surface of TiO_2. As summarized in Table S1,† the intensity ratio between the TiO_2 and CdS diffraction peaks increases with the increase of the TiO_2 feedstock, which indicates that the weight ratio of TiO_2 increases in the order TC-1 < TC-2 < TC-3. According to the ICP results, the TiO_2/CdS mass ratios are calculated to be 2.71, 3.97, and 6.17 for TC-1, TC-2, and TC-3, respectively, following the order TC-1 < TC-2 < TC-3. This is consistent with the XRD results. In the TC-MX composites, the absence of the characteristic diffraction peaks of $Ti_3C_2T_x$ can be ascribed to the very weak diffraction peak of $Ti_3C_2T_x$ itself and the relatively low contents of $Ti_3C_2T_x$.

The morphologies and textural structures of the samples have been investigated by scanning electron microscopy (SEM) and transmission electron microscopy (TEM). As shown in Fig. 1b and Fig. S3,† bare TiO_2 exists as 2D nanosheets with an average width of 50 nm. The lattice spacing in the inset of Fig. 1b is 0.19 nm, corresponding to the (200) crystal plane of anatase TiO_2. The SEM images of TC-1, TC-2, and TC-3 are shown in Fig. S4.† It is seen that TC composites still maintain the 2D morphology of TiO_2, and the surface of the samples becomes rough due to the coating of CdS. Fig. 1c shows the TEM image of TC-2. It shows that nanoparticles are deposited onto the 2D structured TiO_2 nanosheets. These nanoparticles have a lattice spacing of 0.338 nm (the inset of Fig. 1c), corresponding to the (002) facet of hexagonal CdS. In addition, a lattice spacing of 0.19 nm is also observed, which corresponds to the (200) crystal plane of anatase TiO_2. The high-angle annular dark-field (HAADF) scanning TEM (STEM) image of TC-2 and the corresponding energy dispersive X-ray (EDX) maps of Ti, O, Cd, and S are presented in Fig. S5.† It can be seen that the mapping of Ti and O shares a similar margin to that of Cd and S, confirming that CdS is generally distributed on the surface of TiO_2. These results suggest the successful deposition of CdS onto TiO_2. Then $Ti_3C_2T_x$ is introduced to the binary TiO_2@CdS composites. $Ti_3C_2T_x$ is characteristic of 2D nanosheets with a lateral size of hundreds of nanometers, as shown in Fig. S6.† The 2D structure can be clearly distinguished in the SEM image of TC-0.1MX (Fig. S7†). The TEM image provides further information of the microscopic structure of the sample. As shown in Fig. 1d, a lattice spacing of 1.2 nm is observed, which corresponds to the (002) crystal plane of $Ti_3C_2T_x$, indicating that TiO_2@CdS composites are successfully loaded onto the surface of the $Ti_3C_2T_x$ nanosheet. The HAADF STEM image of TC-0.1MX and the corresponding EDX maps of Ti, C, O, Cd, and S are presented in Fig. 1e. It can be seen that Ti shares a similar margin to C, confirming that the substrate is the $Ti_3C_2T_x$ nanosheet. In addition, Ti exhibits a slightly enhanced concentration in the regions identical to the O element, which further indicates that TiO_2 is dispersed on the substrate of $Ti_3C_2T_x$. It is also discernable that the signals of Cd and S accumulate in the TiO_2 region. These results demonstrate that TiO_2@CdS structures interact with the $Ti_3C_2T_x$ substrate driven by electrostatic forces.

The chemical composition and surface states of the samples have been investigated by X-ray photoelectron spectroscopy (XPS). As shown in the XPS survey spectra of TC-0.1MX (Fig. S8a†), Cd, S, Ti, C, and O are presented, which is in coincidence with the EDX mapping results. As shown in Fig. S8b,† C 1s is calibrated with 284.6 eV. The peak at 281.9 eV is ascribed to the C–Ti bond of $Ti_3C_2T_x$, and the peaks at 286.4 and 288.9 eV are ascribed to the C–O and C═O bonds of the existing defects in the carbon layers of $Ti_3C_2T_x$.[46] The binding energies at 529.8 and 531.1 eV are assigned to the O 1s peak of TiO_2[47] and the hydroxyl terminations (–OH) in $Ti_3C_2T_x$ (Fig. S8c†), respectively.[48] As shown in Fig. S8d,† two peaks at 464.2 (Ti $2p_{1/2}$) and 458.6 eV (Ti $2p_{3/2}$) are assigned to Ti(IV) in TiO_2,[47] while the other two at 462.2 (Ti $2p_{1/2}$) and 457.2 eV (Ti $2p_{3/2}$) are from the Ti element in $Ti_3C_2T_x$,[46,48] indicating the successful introduction of $Ti_3C_2T_x$. As for TC-2, the binding energies at 404.5 eV and 411.2 eV are assigned to Cd $3d_{5/2}$ and Cd $3d_{3/2}$, respectively (Fig. 2a). And the binding energies at 160.8 eV and 162.1 eV are assigned to S $2p_{3/2}$ and S $2p_{1/2}$, respectively[47] (Fig. 2b). Noteworthily, the binding energies of Cd and S XPS peaks in TC-0.1MX exhibit a positive shift of 0.2 eV compared to TC-2 (Fig. 2a and b), indicating a decrease of the electron density in CdS. These changes should be ascribed to the electron transfer from CdS to $Ti_3C_2T_x$ due to the Schottky effect between the semiconductor CdS and metallic $Ti_3C_2T_x$.

The optical properties of the samples are shown in Fig. 2c. TC-2 exhibits an extended absorption edge to 541 nm compared to TiO_2 due to the presence of CdS. Notably, with the addition of $Ti_3C_2T_x$, the absorption of the ternary TC-MX composites in the region of 541–1200 nm intensifies compared to TC-2 and increases with the $Ti_3C_2T_x$ content (Fig. 2c). In particular, it is observed that a distinct absorption peak located at about 800 nm appears in the spectra of TC-MX composites. This peak can be ascribed to the LSPR absorption of $Ti_3C_2T_x$.[28,30] Compared to the pure $Ti_3C_2T_x$ aqueous colloids presenting at 780 nm (Fig. S9†), the LSPR peak of $Ti_3C_2T_x$ in TC-MX composites exhibits a red-shift, which should be

 This journal is © The Royal Society of Chemistry 2022

Published on 19 1401. Downloaded on 08/11/1404 05:47:49 ..

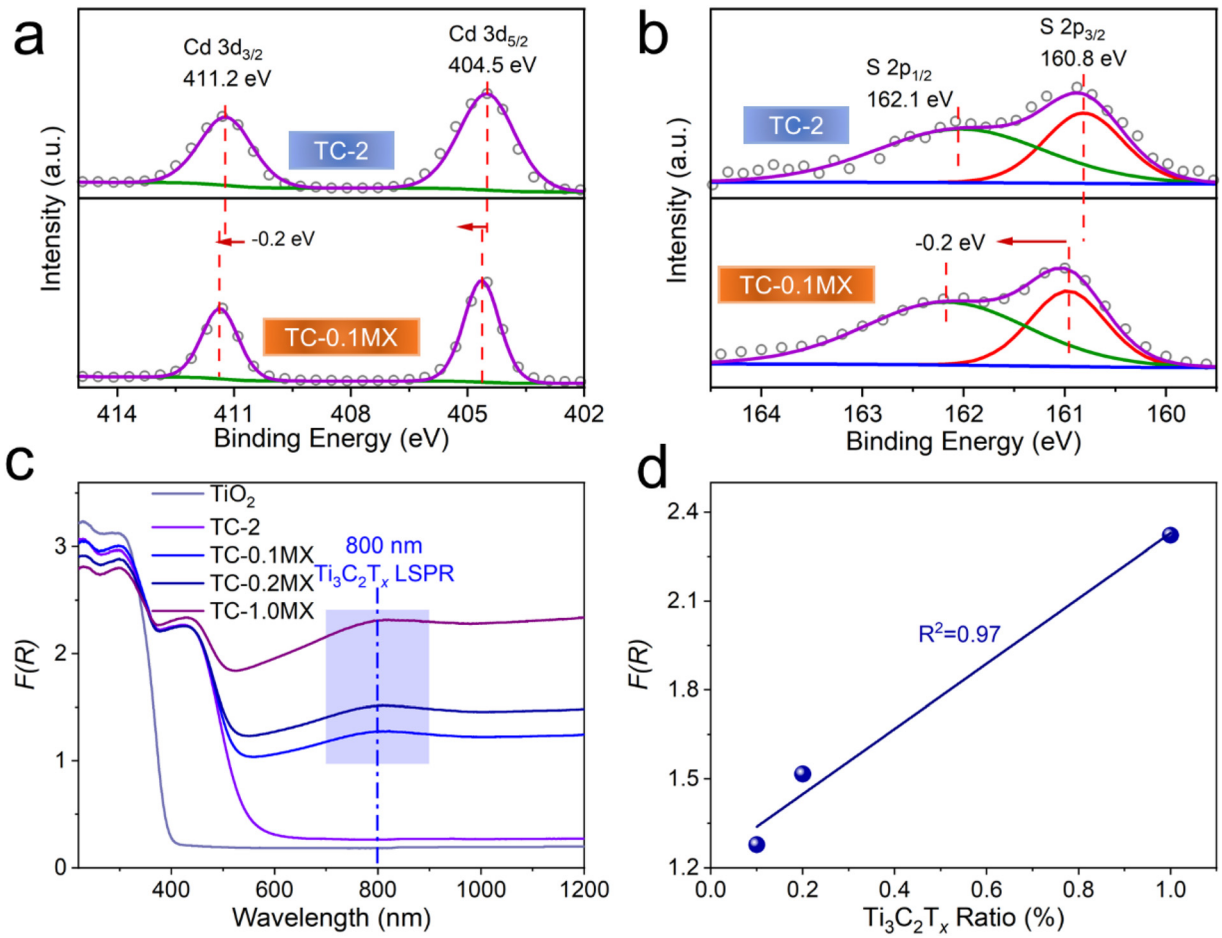

Fig. 2 XPS spectra of TC-2 (top) and TC-0.1MX (bottom): (a) Cd 3d, (b) S 2p. (c) UV-vis diffuse reflectance spectra (DRS) of the samples and (d) plots of absorption at a wavelength of 800 nm *versus* the weight ratio of $Ti_3C_2T_x$ in the TC-MX composites.

ascribed to the high refractive index of the TiO_2 matrix since the LSPR absorption band closely relates to the dielectric constant of the environment.[49,50] Furthermore, the intensity of the absorption peak located at about 800 nm increases almost linearly as a function of the loading of $Ti_3C_2T_x$ in the TC-MX samples, as shown in Fig. 2d. Such an optical absorption feature of $Ti_3C_2T_x$ is distinctively different from its 2D analogue of RGO where only a broad absorption band ranging from the ultraviolet (UV) to the NIR region was observed, as shown in Fig. S10.† In contrast, it is similar to that of traditional metal nanostructures featuring the LSPR effect, such as Au, and Ag.[37–39] The XPS and light absorption results suggest that the introduction of $Ti_3C_2T_x$ affords not only electron interactions between the semiconductors, but also an intriguing LSPR feature. This interesting result has motivated us to evaluate the photocatalytic performances of the samples and investigate the corresponding role of $Ti_3C_2T_x$.

The photocatalytic performances of the samples have been evaluated through the anaerobic selective reduction of aromatic nitro compounds to their corresponding amino compounds, based on the formula expressed in Fig. 3a.[51,52] For the aqueous selective reduction of 4-nitroaniline (4-NA) to 4-phenylenediamine (4-PDA) with the addition of ammonium formate as a hole scavenger and N_2 purging under visible-NIR light irradiation (Fig. S11†), TC-2 exhibits enhanced photoactivity compared to TC-1 and TC-3, as shown in Fig. 3b. According to the Kubelka–Munk function based on the DRS results, the bandgap energy of CdS is calculated to be 2.00 eV (Fig. S12†). The valence band energy (E_{VB}) of CdS determined by the XPS valence band spectrum is 1.03 eV (Fig. S13†). Consequently, the conduction band energy (E_{CB}) is calculated to be −0.97 eV. Considering that the E_{CB} of TiO_2 is calculated to be −0.27 eV (Fig. S14†), the photogenerated electron transfer from CdS to TiO_2 is thermodynamically permissible. This widely explored band alignment effect improves the separation efficiency of photogenerated electron–hole pairs and thus the photoactivity.[53] However, the photoactivity of TC-3 with the further increased TiO_2 ratio is lower than that of TC-2. Photocurrent measurements have been conducted to investigate the charge carrier separation of TC composites. As shown in Fig. S15,† the photocurrent densities follow the order TC-2 > TC-1 > TC-3, which agrees well with the photocatalytic activities. These results show that TC-2 with a decent TiO_2 ratio has the best effect on the spatial separation and transfer of elec-

Published on 19 1401. Downloaded on 08/11/1404 05:47:49 ..

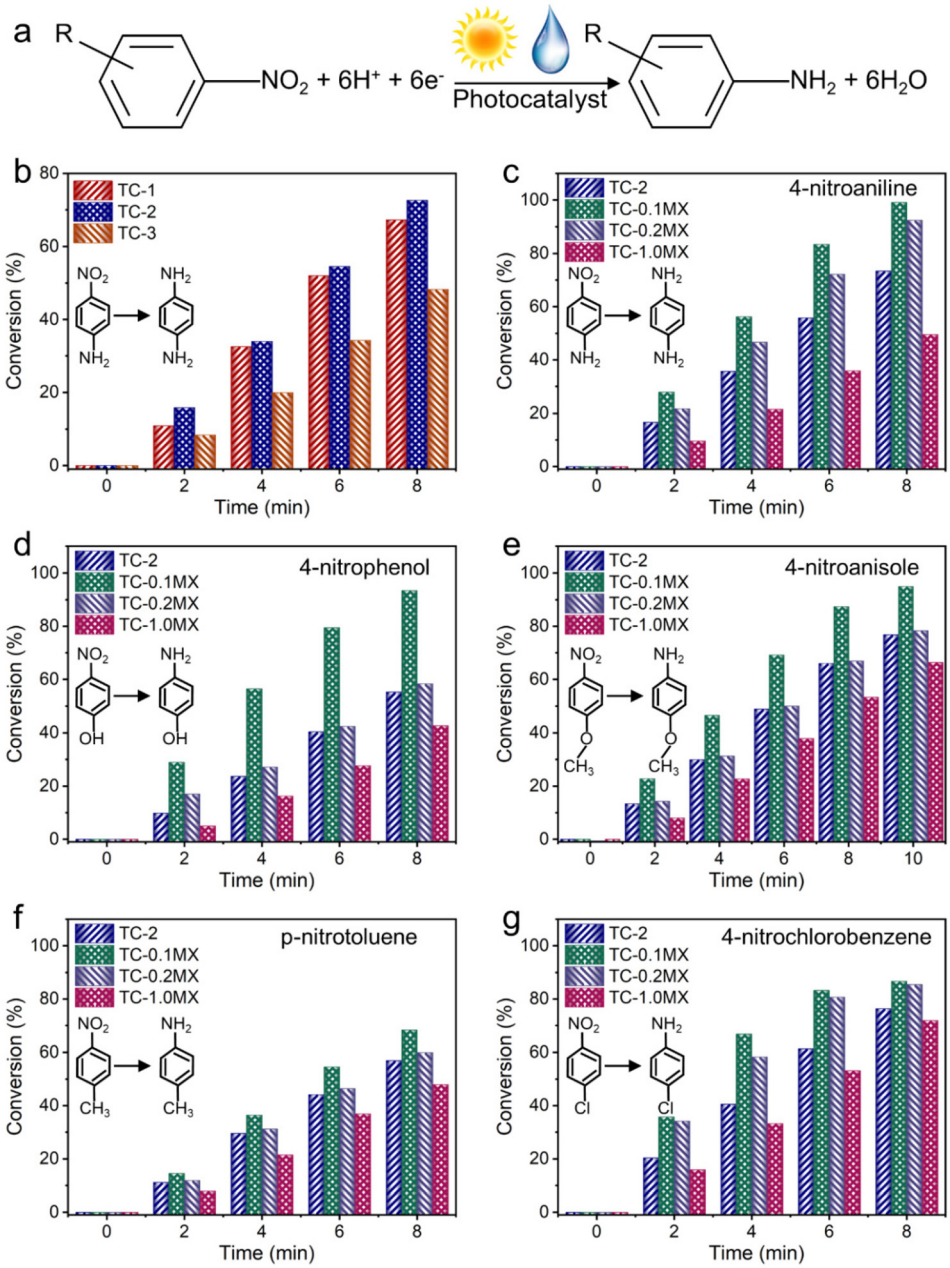

Fig. 3 Photocatalytic performances of different samples. (a) The formula for the photocatalytic reduction of nitroaromatics to the corresponding amino compounds. (b) Photocatalytic activities of TC composites for the selective reduction of 4-nitroaniline (4-NA) to 4-phenylenediamine (4-PDA) in water with the addition of ammonium formate as a hole scavenger and N_2 purging in water under visible-NIR light irradiation (λ > 420 nm). Photocatalytic activities of TC-2, TC-0.1MX, TC-0.2MX and TC-1.0MX for the selective reduction of (c) 4-nitroaniline, (d) 4-nitrophenol, (e) 4-nitroanisole, (f) *p*-nitrotoluene, and (g) 4-nitrochlorobenzene.

tron–hole pairs in the binary TC system. The introduction of $Ti_3C_2T_x$ with appropriate ratios into TC-2 leads to the further improved photoactivity. It can be seen from Fig. 3c that the ternary TC-0.1MX exhibits better photoactivity than TC-2 for the reduction of 4-NA to 4-PDA. Compared to TC-0.1MX, TC-0.2MX and TC-1.0MX with further increased $Ti_3C_2T_x$ weight ratios exhibit decreased photoactivity. A similar phenomenon has been widely reported previously, which could be ascribed to the "light-shielding effect" of $Ti_3C_2T_x$.[25] For comparison, TC-2 has also been hybridized with RGO of 0.1 at% and 0.2 at%, which are denoted as TC-0.1RGO and TC-0.2RGO, respectively. The photocatalytic performances of these samples have also been evaluated under the same conduction conditions as those for TC-MX. As shown in Fig. S16,† both TC-0.1MX and TC-0.2MX exhibit enhanced photocatalytic activity compared to the counterparts of TC-0.1RGO and TC-0.2RGO. In addition, control experiments have been performed for the photoreduction of nitroaromatics as shown in Fig. S17.†

This journal is © The Royal Society of Chemistry 2022

Published on 19 1401. Downloaded on 08/11/1404 05:47:49 ..

Specifically, experiments without photocatalysts or light irradiation show no conversion, indicating that the reaction is a photocatalytic process. The photocatalytic reduction of 4-NA over TC-0.1MX decreased dramatically without N_2, indicating that the inert atmosphere is indispensable for the photocatalytic reduction of 4-NA.[54,55] Furthermore, when employing $K_2S_2O_8$ as a scavenger for photogenerated electrons, only weak activity has been observed, confirming that the photoreduction reaction of nitroaromatics is decisively driven by electrons.[50] In addition, the experiment in the dark excludes the influence of 4-NA adsorption on the photocatalytic performance (Fig. S18†). Fig. S19† displays the resilience of the photocatalytic activity of the TC-0.1MX composite toward the selective reduction of 4-NA under visible-NIR irradiation, which remains relatively stable after three cycles. It can be seen from Fig. S20 and S21† that the morphology and crystal phase structure of TC-0.1MX remained unchanged after three cycles of photocatalytic reaction, indicating that the material has good stability. An identical progressive photoactivity variation has also been found for the selective reduction of a wide range of aromatic nitro compounds, including 4-nitroaniline, 4-nitrophenol, 4-nitroanisole, *p*-nitrotoluene, and 4-nitrochlorobenzene, as shown in Fig. 3d–g. These confirm the essential role of $Ti_3C_2T_x$ in enhancing the photocatalytic performance of the composites.

To gain deep insight into the underlying mechanism of $Ti_3C_2T_x$ enhanced photoactivity, a series of joint electrochemical measurements, optical analysis, and simulations have been carried out. The previous XPS results (Fig. 2a and b) show that there is an obvious Schottky effect between CdS and $Ti_3C_2T_x$, which can be understood by the band structure analysis. As discussed above, the conduction band (E_{CB}) of CdS determined by the DRS and the XPS valence band spectrum results is at −0.97 eV. Ultraviolet photoelectron spectra (UPS) have been employed to measure the work function of $Ti_3C_2T_x$. As shown in Fig. S22,† the work function of metallic $Ti_3C_2T_x$ is calculated to be 4.31 eV, indicating that it is feasible for highly electrically conductive $Ti_3C_2T_x$ (2000 S cm^{-1}) to accept the electrons photogenerated from CdS and construct Schottky heterojunctions, thus inhibiting the recombination of photogenerated charge carriers. In addition, the E_F of $Ti_3C_2T_x$ is calculated to be −0.13 V (*versus* NHE), which is more positive than the E_F of CdS. This suggests that it is feasible for $Ti_3C_2T_x$ to accept the photogenerated electrons on CdS. Mott–Schottky plots have been measured to ascertain the detail of the energy band of TC-2 and TC-0.1MX composites. As shown in Fig. S23,† the Mott–Schottky plots with positive slopes are observed, which is consistent with the typical feature of n-type semiconductors.[56] The flat band potential (E_{FB}) of TC-2 is −0.54 V *versus* Ag/AgCl (equivalent to −0.34 V *versus* standard hydrogen electrode, NHE), which shifts positively to −0.37 V *versus* Ag/AgCl (equivalent to −0.17 V *versus* NHE) for TC-0.1MX. Considering that the E_{FB} measured by the Mott–Schottky relationship is equal to the Fermi level (E_F) for n-type semiconductors,[56] the more positive E_{FB} of TC-0.1MX than that of TC-2 should result from the Fermi-level equilibration of the different components, which further confirms the "electron reservoir" effect of $Ti_3C_2T_x$ due to the Schottky contact.

The LSPR absorption peak of $Ti_3C_2T_x$ has been identified from the aforementioned DRS results. The interesting light conversion capability by the LSPR effect of $Ti_3C_2T_x$ has intrigued the exploration of photothermal conversion and photodetectors,[32,36] while the application of photocatalysis has not been known clearly. This motivates us to investigate the contribution of the LSPR effect to the enhanced photoactivity of the ternary TC-MX composites compared to the binary TC composites. It has been recognized that the traditional LSPR metals are capable of enhancing photocatalysis by hot electron injection.[57] In this regard, while keeping other reaction parameters unchanged, the photocatalytic performance for the reduction of 4-NA has been tested under the irradiation of $\lambda >$ 780 nm, by which only $Ti_3C_2T_x$ LSPR is excited. Under such conditions, only 4% of 4-NA is converted over TC-0.1MX (Fig. S24†), which is far less than that over TC-0.1MX (100%) under the visible-NIR light irradiation of $\lambda >$ 420 nm (Fig. 4a), suggesting that the hot electron injection effect by $Ti_3C_2T_x$ has a negligible effect on promoting the photocatalytic reduction of 4-NA. Otherwise, when the same weight of pure $Ti_3C_2T_x$ in TC-0.1MX acts as a direct catalyst, almost no photoactivity is observed for the probe reaction (Fig. 4a), which suggests that the plasmonic $Ti_3C_2T_x$ does not serve as the direct photocatalyst in our current reaction system. Previous investigation reports that the $Ti_3C_2T_x$ plasmon-induced thermalization increases the local temperature to 66 °C.[28] Although the reaction temperature has been controlled at room temperature by circulating water in our current research, the possible local temperature elevation due to the efficient light-to-heat conversion of plasmonic $Ti_3C_2T_x$ remains suspicious for enhancing the photocatalysis. In this circumstance, control experiments at elevated temperatures have been performed. Fig. 4b shows that the photocatalytic activity of TC-2 decreases with the increase of reaction temperature, which may be ascribed to the increased probability of photogenerated charge carrier recombination as the temperature increases.[58] This result excludes the influence of $Ti_3C_2T_x$ assisted photothermal catalysis on promoting the photoactivity of TC-0.1MX composites. Considering that the LSPR effect can result in enhanced electric fields, the finite-difference time-domain (FDTD) simulations were further carried out to simulate the electric field ($|E|/|E_0|$) distributions based on the model shown in Fig. S25.† As displayed in Fig. 4c, a significant enhancement of the electric field for TC-0.1MX is observed compared to that of TC-2, which matches well with the FDTD results for bare $Ti_3C_2T_x$ (Fig. S26†). These results confirm that the electric field enhancement originates from $Ti_3C_2T_x$. It is noted that the electric field enhancement is mainly observed on the edge of $Ti_3C_2T_x$. The reason could be that the free carriers are confined to the edge of the nanosheet by photon excitation in the direction parallel to $Ti_3C_2T_x$.[34,37] Furthermore, Fig. 4d shows the Raman spectroscopy of TC-2 and TC-0.1MX. The peaks at 143, 218, 390, 472, 514, and 636 cm^{-1} correspond to the anatase

Published on 19 1401. Downloaded on 08/11/1404 05:47:49 ..

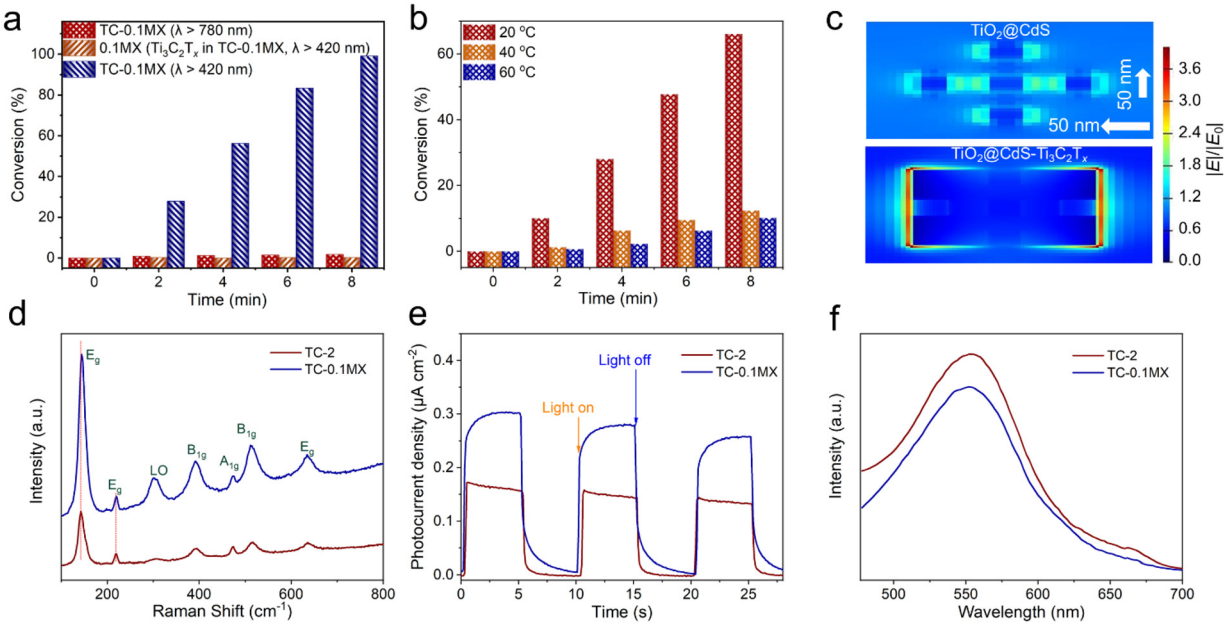

Fig. 4 Mechanism analysis of $Ti_3C_2T_x$-enhanced photocatalysis. (a) Photocatalytic activities for the selective reduction of 4-NA. (b) Photoactivities of TC-0.1MX for the selective reduction of 4-NA under visible-NIR light irradiation (λ > 420 nm) at different temperatures. (c) Local electric field distributions of TiO_2@CdS and TiO_2@CdS–$Ti_3C_2T_x$ composites calculated by the finite-difference time-domain (FDTD) method. (d) Raman spectra of TC-2 and TC-MX composites. (e) Photocurrent densities of TC-2, TC-0.1MX under visible-NIR light irradiation (λ > 420 nm). (f) Photoluminescence (PL) emission spectra of TC-2 and TC-0.1MX.

TiO_2 Raman modes of E_g, E_g, B_{1g}, B_{1g}, A_{1g}, and E_g,[59] respectively, and the peak at 305 cm^{-1} belongs to the CdS Raman mode of LO.[60] It is noteworthy that the Raman intensity of TC-0.1MX is stronger than that of TC-2. According to the principle of surface-enhanced Raman spectroscopy (SERS), the plasmon-induced local electromagnetic field can significantly enhance the intensity of Raman signals.[61] Consequently, compared with TC-2, the enhancement of Raman signals in TC-0.1MX further corroborates the $Ti_3C_2T_x$ plasmon-induced local electromagnetic field, which can promote the separation of electron–hole pairs in nearby semiconductors, thereby leading to a higher photocatalytic activity. Moreover, the Eg modes of TC-0.1MX have a slight blue shift compared to TC-2, which is ascribed to the carrier density modulation induced by charge transfer between TC-2 and $Ti_3C_2T_x$.[62–64] Furthermore, the photo-induced charge carrier density over the composites has been estimated by the Mott–Schottky analysis under 1 sun irradiation. The photo-induced charge carrier density (N_D) is calculated to be 3.7×10^{19} cm^{-3} and 7.5×10^{19} cm^{-3} from the slope of $1/C^2$ *vs.* V for TC-2 and TC-0.1MX, respectively (Fig. S27†). Thus, the joint experiments indicate that the LSPR enhancement mechanisms should be interpreted in terms of the electric field enhancement effect, which has a significant positive effect on the separation of photogenerated carriers. To the best of our knowledge, this is the first report on the electric field enhancement induced by the LSPR effect of $Ti_3C_2T_x$ in the field of photocatalysis. Studies have shown that the shape, size, layer thickness and the surface terminal groups of $Ti_3C_2T_x$ have a great impact on the LSPR absorption band of $Ti_3C_2T_x$, and the LSPR light absorption band of $Ti_3C_2T_x$ can reach about 2400 nm.[40] This further unleashes the possibilities of using the LSPR effect to develop efficient $Ti_3C_2T_x$-based plasmonic materials to enhance photoredox catalysis.

As shown in Fig. 4e, the photocurrent intensity of TC-0.1MX is higher than that of TC-2, suggesting that the separation of photogenerated charge carriers over TC-0.1MX is more efficient than that over TC-2. This is further verified by the weaker photoluminescence (PL) intensity of TC-0.1MX than that of TC-2 (Fig. 4f), confirming the inhibited recombination of photogenerated charge carriers by $Ti_3C_2T_x$. As shown in Fig. S28,† the average fluorescence lifetime increases from 0.53 ns (TC-2) to 0.62 ns (TC-0.1MX), confirming that the introduction of $Ti_3C_2T_x$ to TC can efficiently accelerate the spatial charge separation and inhibit the charge recombination, and thus prolong the lifetime of photogenerated charge carriers. The open circuit photovoltage (OCP) decay technique has been used to measure the lifetime of photoelectrons under visible-NIR light irradiation (Fig. S29†), from which it is clearly seen that the photoelectron lifetime of TC-0.1MX is longer than that of binary TC-2. In addition, the Nyquist diagrams show that the TC-0.1MX electrode has a smaller semicircle at high frequencies compared to TC-2 (Fig. S30†), suggesting that the introduction of metallic $Ti_3C_2T_x$ contributes to the enhanced charge transfer process. This is further verified by the cyclic voltammetry (CV) results, where TC-0.1MX exhibits a higher current density than TC-2 (Fig. S31†). Based on these results, the introduction of $Ti_3C_2T_x$ affords not only the "electron reservoir" effect, but also local electric field enhancement due

 This journal is © The Royal Society of Chemistry 2022

Published on 19 1401. Downloaded on 08/11/1404 05:47:49 ..

to the LSPR effect, which cooperatively enhance the separation and transfer of photogenerated charge carriers.

As such, compared to the unidirectional electron transfer controlled by the band-alignment effect in the binary TiO_2@CdS, additional transfer pathways of photogenerated electrons in CdS have been established for the ternary TiO_2@CdS–$Ti_3C_2T_x$. The multichannel electron transfer pathway in TiO_2@CdS–$Ti_3C_2T_x$ is consolidated by *in situ* irradiated X-ray photoelectron spectroscopy (ISI-XPS). As shown in Fig. 5a, for the experiment without light irradiation, two XPS peaks located at 404.8 and 411.5 eV are observed, which are assigned to Cd $3d_{5/2}$ and Cd $3d_{3/2}$, respectively.[47] Under light irradiation, the Cd 3d XPS peaks exhibit a positive shift of 0.4 eV. Analogously, a positive shift of the S 2p peaks has also been observed after the visible-NIR light irradiation (Fig. 5b), suggesting the electron depletion on CdS. For the Ti 2p XPS spectrum without light irradiation, two peaks at 464.5 (Ti $2p_{1/2}$) and 458.8 eV (Ti $2p_{3/2}$) are assigned to Ti(IV) in TiO_2, while the other two at 462.9 (Ti $2p_{1/2}$) and 457.5 eV (Ti $2p_{3/2}$) are from the Ti element in $Ti_3C_2T_x$[48] (Fig. 5c). Meanwhile, two peaks at 531.5 and 530.0 eV are attributed to the hydroxyl terminations (–OH) in $Ti_3C_2T_x$ and the lattice O in TiO_2,[48] as shown in Fig. 5d. Under visible-NIR light irradiation, there is an apparent negative shift of the binding energies of Ti 2p XPS peaks, *i.e.*, −0.1 eV for TiO_2 and −0.3 eV for $Ti_3C_2T_x$. Similar decreased binding energies are observed for the O 1s XPS peaks upon visible-NIR light irradiation, indicating the accumulation of electrons on both TiO_2 and $Ti_3C_2T_x$ under visible-NIR light irradiation. These shifts of binding energies provide direct evidence of the photogenerated electron transfer pathways across the TC-0.1MX interface under the same visible-NIR light irradiation conditions as the photocatalytic reaction. Specifically, the photogenerated electrons from the irradiated CdS can migrate to both TiO_2 and $Ti_3C_2T_x$, thus affording multichannel electron transfer pathways for the separation of photogenerated electron–hole pairs toward enhancing the photoactivity. The electron density difference is further calculated to study the charge transfer process in the TC-0.1MX interface, as shown in Fig. 5e and Fig. S32.† The green and yellow regions depict electron accumulation and depletion regions, respectively. The charge accumulation primarily occurs at the interfaces between CdS and $Ti_3C_2T_x$, and between CdS and TiO_2. The obvious electron transfer process can also be observed (isovalue = 0.03) in Fig. 5e. According to the Hirshfeld charge analysis,[65] 1.67 e^- can transfer from CdS to $Ti_3C_2T_x$, and 0.13 e^- can transfer from CdS to TiO_2, respectively. It is anticipated that under light irradiation, the photoinduced electrons will accumulate in $Ti_3C_2T_x$ and TiO_2. This further confirms the multichannel electron transfer pathway in the hole–electron charge separation process and is consistent with the ISI-XPS characterization.

Based on the above analysis, a mechanism of multichannel charge transfer enhanced photoactivity for the reduction of nitroaromatics over the ternary TiO_2@CdS–$Ti_3C_2T_x$ is proposed, as illustrated in Fig. 6. Under visible-NIR light irradiation (λ > 420 nm), photoinduced electron–hole pairs are generated in CdS, which follow band alignment-mediated charge transfer as the electrons in the CB of CdS are transferred to the CB of TiO_2. Meanwhile, $Ti_3C_2T_x$ acts as the "electron reservoir" due to the Schottky junction between CdS and $Ti_3C_2T_x$, which further captures and transfers the excited electrons in the CB of CdS, resulting in an efficient spatial separ-

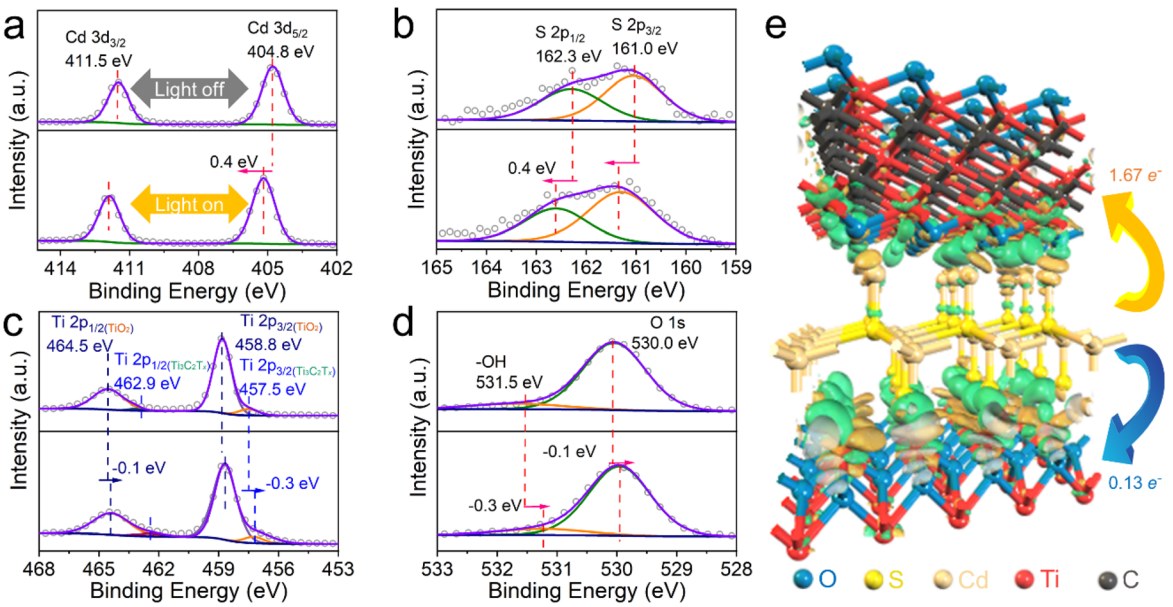

Fig. 5 ISI-XPS characterization and DFT calculations of TC-0.1MX. (a) Cd 3d, (b) S 2p, (c) Ti 2p, and (d) O 1s XPS spectra in the dark (top) and under visible-NIR light irradiation of λ > 420 nm (bottom). (e) The electron density difference of TC-MX. Forest green and yellow regions indicate accumulation and depletion of electrons, respectively.

Published on 19 1401. Downloaded on 08/11/1404 05:47:49 ..

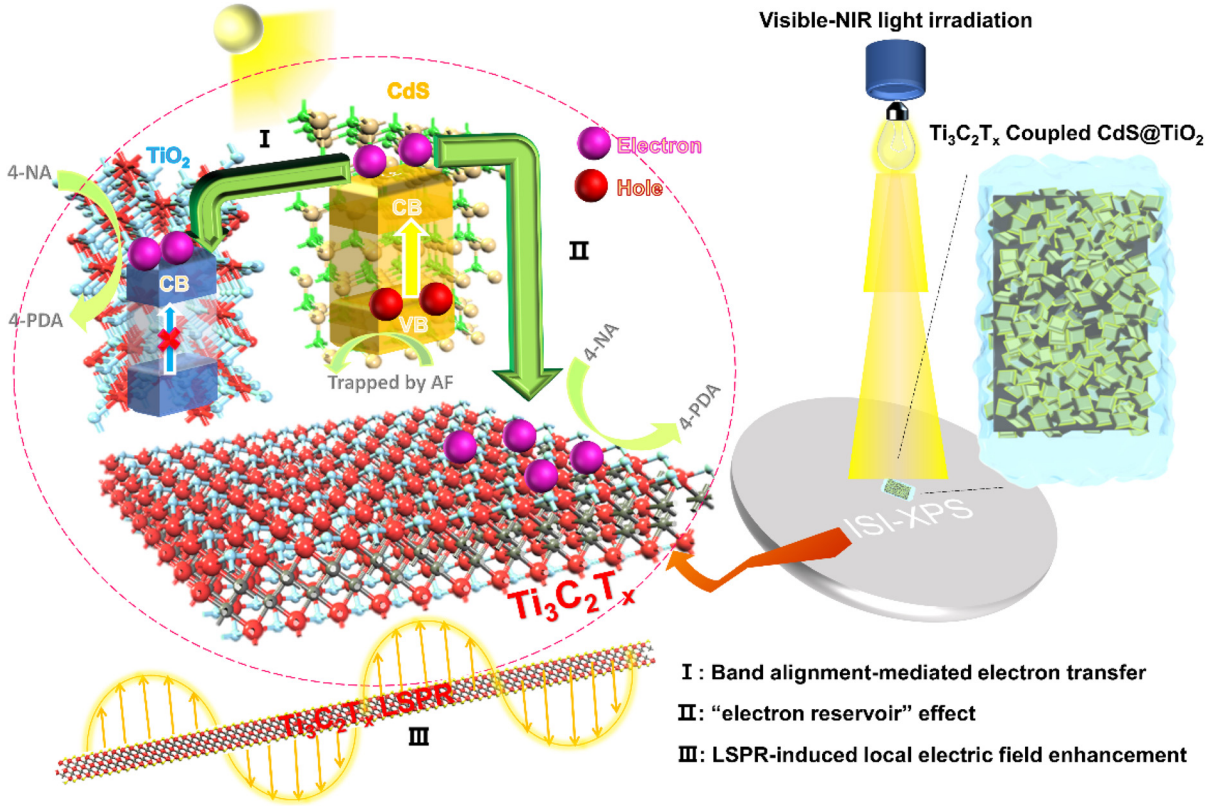

Fig. 6 Illustration of the proposed reaction mechanism for the photocatalytic reduction of nitroaromatics over TC-0.1MX under visible-NIR light irradiation (λ > 420 nm) with the addition of ammonium formate (AF) as a hole scavenger and N_2 purging in water.

ation of photoinduced charge carriers. Besides, the LSPR effect of $Ti_3C_2T_x$ enables local electric field enhancement to further boost the separation of charge carriers in CdS. As a result, the photogenerated electrons produced by CdS are efficiently extracted and the photocatalytic activity toward the reduction of nitroaromatics is enhanced.

3. Conclusions

In summary, taking TiO_2@CdS as a typical heterostructured photocatalyst, we have demonstrated $Ti_3C_2T_x$ as a dual-functional cocatalyst for steering photogenerated electron flow for enhanced photoredox catalysis. Our investigations clearly reveal that $Ti_3C_2T_x$ with a high work function behaves as an "electron reservoir" due to the Schottky-junction effect, which is beneficial for suppressing the recombination of photogenerated electron–hole pairs. Of particular interest is that $Ti_3C_2T_x$ exhibits the typical LSPR effect, which induces local electric field enhancement to boost the separation efficiency of electron–hole pairs. With these advantages integrated, the introduction of $Ti_3C_2T_x$ affords multiple electron transfer pathways in the TiO_2@CdS–$Ti_3C_2T_x$ composite photocatalysts. Our findings shed light on the knowledge of the versatility of $Ti_3C_2T_x$ in enhancing photoredox catalysis, making it much more viable for constructing multicomponent photocatalysts with multichannel charge transfer pathways for the activation and reduction of appealing small molecules, such as CO_2 and N_2.

4. Experimental methods

4.1. Materials

All used chemicals were obtained from commercial suppliers without further purification. Sublimed sulfur (S_8), cadmium chloride ($CdCl_2{\cdot}2.5H_2O$), methanol (CH_4O), ethanol (C_2H_6O), hydrochloric acid (HCl), ammonium formate (AF), and *N*,*N*-dimethylformamide (DMF) were obtained from Sinopharm Chemical Reagent Co., Ltd (Shanghai, China). Butyl titanate (TBT), hydrogen fluoride (HF) and lithium fluoride (LiF) were obtained from Aladdin Industrial Corporation. Titanium aluminium carbide 312 (Ti_3AlC_2) powder was obtained from FoShan XinXi Technology Co., Ltd. Deionized (DI) water used throughout the whole experiments was obtained from ultrapure water production apparatus. Fluorine-doped tin oxide (FTO)-coated glass substrates were purchased from Wuhan Jinge-Solar Energy Technology Co., Ltd.

4.2. Catalyst preparation

4.2.1 Synthesis of TiO_2 nanosheets. In a typical preparation, 5 mL of TBT and 1 mL of HF were mixed under mild stirring, which was transferred to a 100 mL Teflon-lined stain-

 This journal is © The Royal Society of Chemistry 2022

Published on 19 1401. Downloaded on 08/11/1404 05:47:49 ..

less-steel autoclave. The autoclave was sealed and maintained at 180 °C for 24 h, after which it was allowed to cool down naturally to room temperature. The white product recovered by centrifugation was washed with DI water and anhydrous ethanol several times and dried at 60 °C for 12 h.

4.2.2 Synthesis of TiO_2@CdS binary composites. 80 mg of $CdCl_2{\cdot}2.5H_2O$ and 20 mg of S_8 were ultrasonically dispersed in 50 mL of methanol to form a suspension, which was bubbled with N_2 for 30 min in the dark. Then, 50 mg of TiO_2 nanosheets was added into the suspension, which was then irradiated using a 300 W xenon lamp for 1 h under a N_2 atmosphere. Finally, the obtained samples were washed with deionized water and dried in an oven at 60 °C, generating TC-1. TC-2 and TC-3 were prepared similarly except that 100 and 200 mg of TiO_2 nanosheets was added.

4.2.3 Construction of TiO_2@CdS–$Ti_3C_2T_x$. $Ti_3C_2T_x$ colloid solution was prepared according to the previous literature.[17] 40 mg of TC-2 was dispersed in 20 mL of DI by ultrasonication, and then a certain volume of $Ti_3C_2T_x$ colloid solution (80, 160, and 800 μl) with a concentration of 0.5 mg mL^{-1} was added to the above suspension, which was then mixed under intense agitation at 800 rpm for 1 min. The above solutions were tested for photocatalytic reactions directly.

4.3. Material characterization

For zeta potential measurements, 1 mg samples were added to 1 mL DI water, and sonicated to disperse evenly. The above solution was dropped into the Malvern zeta potential sample cell and zeta potential measurements of the samples were conducted on a Zetasizer Nano ZSP. The X-ray diffraction patterns of the samples were measured on a MiniFlex 600 X-ray diffractometer using Ni-filtered Cu Kα radiation at a scan rate of 5° min^{-1}. The mass proportions of Ti and S in TC samples were measured by Inductively Coupled Plasma Optical Emission Spectroscopy (ICP-OES) (Agilent, ICP-OES 730). Raman spectra were recorded on a laser confocal inverted microscope Raman spectrometer (inVia-reflex) with a 633 nm laser as an excitation source. Scanning electron microscopy (SEM, S4800, Hitachi S-4800) was performed to determine the morphology of the samples. TEM images, high-resolution TEM (HRTEM) images, and elemental mapping results were obtained on a field emission transmission electron microscope with spherical aberration correction of the objective lens (Titan G2 60-300) at an acceleration voltage of 300 kV. X-ray photoelectron spectroscopy (XPS) measurements were performed using an AXIS SUPRA, and ultraviolet photoelectron spectroscopy (UPS) measurements were performed with He I (21.22 eV) as a monochromatic light source. *In situ* irradiated X-ray photoelectron spectroscopy (ISI-XPS) was conducted on a Thermo Fisher Escalab 250xi with an Al Kα radiation hemispherical electron energy analyzer and a 300 W Xe arc lamp (Microsolar300A, Beijing Perfect Light Co., Ltd) with a 420 nm cut-off filter being placed *ca.* 20 cm away from the prepared samples during the ISI-XPS characterization to investigate the electron density changes of the samples under visible-NIR light irradiation (λ > 420 nm). All binding energies were calibrated with the C 1s peak at 284.6 eV. The electrical conductivity of the MXene films was measured using a four-point probe setup (4 PROBES TECH) with a uniform 1.0 mm probe spacing. A Shimadzu UV-vis near-infrared spectrometer was used to measure the optical properties of the samples. The photoluminescence (PL) spectra for samples were analyzed on an Edinburgh FLS9800 with an excitation wavelength of 375 nm.

4.4. Electrochemical measurements

The electrochemical analysis was carried out in a conventional three electrode cell, which uses an Ag/AgCl electrode as the reference electrode and a Pt plate as the counter electrode on an electrochemical workstation (Shanghai Chenhua, CHI600E). Fluorine-doped tin oxide (FTO) glasses were used as the substrate for the working electrode, which were cleaned by sonication in absolute ethanol for 30 min and dried at 60 °C. The conductive surface of the FTO glass was covered with cellophane with a 0.5 mm hole near the end. 5 mg of sample was ultrasonically dispersed in 0.5 mL of DMF, and then 20 μl of the above dispersions was dropped on the pretreated FTO glass. After drying at room temperature, the cellophane was removed and the uncoated area of the FTO glass was protected with nail polish glue. The photocurrent measurement was performed under visible-NIR light irradiation (>420 nm), and the open circuit photovoltage decay (OCP) measurements were conducted under visible-NIR light irradiation for 60 s and then the subsequent decay of photovoltage was monitored for 50 s with the light turned off, and the Mott–Schottky (M–S) experiments were obtained in 0.2 M Na_2SO_4 aqueous solution at 300 Hz. The electrochemical impedance spectroscopy (EIS) experiments were performed in 0.5 M KCl containing 0.01 M $K_3[Fe(CN)_6]/K_4[Fe(CN)_6]$ in a frequency range from 1 Hz to 100 kHz under open-circuit potential conditions. Cyclic voltammograms (CV) were collected in the same electrolyte at a scan rate of 0.09 mV s^{-1}.

4.5. FDTD simulations and theoretical calculations

The electric field simulation was performed using the Finite Differential Time Domain (FDTD) software package (Lumpolishing Solutions, Inc.). The refractive indices of $Ti_3C_2T_x$, TiO_2, and CdS were obtained from previously reported data.[66] The total field/scattered field (TFSF) light source was used as the incident field in the simulation area. The wavelength of the incident field was consistent with that of the experimental radiation source. The perfect matching layer (PML) boundary conditions were used in the simulation. The length of $Ti_3C_2T_x$ in the long direction is 340 nm and the width is 205 nm. TiO_2@CdS is a square with a length of 55 nm and a thickness of 3.81 nm. For the model of TiO_2@CdS–$Ti_3C_2T_x$, the middle position of each of the four edges and the center of the $Ti_3C_2T_x$ sheet is loaded with TiO_2@CdS.

The density functional theory (DFT) calculations are carried out using the CASTEP code[2] for this work.[65] The generalized gradient approximation (GGA) with the Perdew–Burke–Ernzerhof (PBE) functional is used to describe the electronic exchange and correlation effects,[67] and the plane-wave cutoff is tested and set to 571.4 eV. The self-consistent field (SCF) tol-

Published on 19 1401. Downloaded on 08/11/1404 05:47:49 ..

erance is 1×10^{-6} eV. The core electrons are treated with ultrasoft pseudo-potentials.

4.6. Photoactivity measurements

40 mg of catalyst and 40 mg of ammonium formate (AF) were mixed with 20 mL of aromatic nitro compounds (50 ppm) in a glass reactor. Before irradiation, the mixture was stirred for 30 min and bubbled with N_2 for another 30 min in the dark to ensure the adsorption–desorption equilibrium between the sample and the reactant. In a typical test, the glass reactor was irradiated with a 300 W Xe arc lamp (PLS-XSE300d) with a 420 nm cut-off filter and the distance between the lamp holder and the photocatalytic reactor was 0.5 cm. 2 mL of the sample solution was collected at regular time intervals, centrifuged (8000 rpm) and the supernatant was analyzed using a UV-vis spectrophotometer (Shimadzu, UV-1780).

The photocatalytic performance of the aromatic nitro compounds was calculated using the conversion equation as follows:

$$\text{Conversion} = \left(1 - \frac{C_t}{C_0}\right) \times 100\%$$

where C_0 is the initial concentration of aromatic nitro compounds after the establishment of the adsorption–desorption equilibrium before the photocatalytic reaction, and C_t is the concentration of aromatic nitro compounds at intervals of two minutes after irradiation.

Author contributions

N. Zhang and X. Xie conceived the research. G. Xie, X. Wang and J. Wang prepared photocatalysts and conducted all the experiments. C. Han performed the FDTD calculations. F. Song, Y. Zhu and Z. Wu offered help to analyse the characterization results. G. Xie, X. Xie and N. Zhang wrote and revised the manuscript. All authors provided critical feedback and assisted during manuscript preparation.

Conflicts of interest

The authors declare that they have no known competing financial interests or personal relationships that could have appeared to influence the work reported in this paper.

Acknowledgements

This work was supported by the National Natural Science Foundation of China (52272295, 52071137, 51977071, 51802040, and 21802020), the Science and Technology Innovation Program of Hunan Province (2021RC3066 and 2021RC3067) and the Natural Science Foundation of Hunan Province (2020JJ3004 and 2020JJ4192). N. Zhang and X. Xie also acknowledge the financial support of the Fundamental Research Funds for the Central Universities.

References

1 S. Li, J. Xiong, X. Zhu, W. Li, R. Chen and G. Cheng, *J. Mater. Sci. Technol.*, 2022, **101**, 242–263.
2 Z. Q. Wei, S. Hou, X. Lin, S. Xu, X. C. Dai, Y. H. Li, J. Y. Li, F. X. Xiao and Y. J. Xu, *J. Am. Chem. Soc.*, 2020, **142**, 21899–21912.
3 K. L. J. Prather, *Nat. Catal.*, 2020, **3**, 181–183.
4 W. Lei, T. Zhou, X. Pang, S. Xue and Q. Xu, *J. Mater. Sci. Technol.*, 2022, **114**, 143–164.
5 C. Wan, J. Jin, X. Wei, S. Chen, Y. Zhang, T. Zhu and H. Qu, *J. Mater. Sci. Technol.*, 2022, **124**, 102–108.
6 Z. Jiang, B. Cheng, Y. Zhang, S. Wageh, A. A. Al-Ghamdi, J. Yu and L. Wang, *J. Mater. Sci. Technol.*, 2022, **124**, 193–201.
7 Q. Xu, S. Wageh, A. A. Al-Ghamdi and X. Li, *J. Mater. Sci. Technol.*, 2022, **124**, 171–173.
8 Z. Jin, J. Li, Y. Zhang, D. Liu, H. Ding, B. B. Mamba, A. T. Kuvarega and J. Gui, *J. Mater. Sci. Technol.*, 2022, **125**, 38–50.
9 X. Ren, C. Wei, Y. Sun, X. Liu, F. Meng, X. Meng, S. Sun, S. Xi, Y. Du, Z. Bi, G. Shang, A. C. Fisher, L. Gu and Z. J. Xu, *Adv. Mater.*, 2020, **32**, 1–13.
10 Y. Cui, X. Tan, K. Xiao, S. Zhao, N. M. Bedford, Y. Liu, Z. Wang, K. H. Wu, J. Pan, W. H. Saputera, S. Cheong, R. D. Tilley, S. C. Smith, J. Yun, L. Dai, R. Amal and D. W. Wang, *ACS Energy Lett.*, 2020, **5**, 3560–3568.
11 W. Xi, K. Wang, Y. Shen, M. Ge, Z. Deng, Y. Zhao, Q. Cao, Y. Ding, G. Hu and J. Luo, *Nat. Commun.*, 2020, **11**, 1–8.
12 X. Sun, S. R. Dawson, T. E. Parmentier, G. Malta, T. E. Davies, Q. He, L. Lu, D. J. Morgan, N. Carthey, P. Johnston, S. A. Kondrat, S. J. Freakley, C. J. Kiely and G. J. Hutchings, *Nat. Chem.*, 2020, **12**, 560–567.
13 C. Chen, Y. Zhu, M. Tian, Y. Chen, Y. Yang, K. Jiang and S. Gao, *Nano Energy*, 2021, **81**, 105623.
14 J. Song, S. Liu, C. Yang, G. Wang, H. Tian, Z. Zhao, R. Mu and J. Gong, *Appl. Catal., B*, 2020, **263**, 118367.
15 J. Lu, J. Wang, Q. Zou, D. He, L. Zhang, Z. Xu, S. He and Y. Luo, *ACS Catal.*, 2019, **9**, 2177–2195.
16 J. Zhang, N. Kong, S. Uzun, A. Levitt, S. Seyedin, P. A. Lynch, S. Qin, M. Han, W. Yang, J. Liu, X. Wang, Y. Gogotsi and J. M. Razal, *Adv. Mater.*, 2020, **32**, 2001093.
17 C. E. Shuck, A. Sarycheva, M. Anayee, A. Levitt, Y. Zhu, S. Uzun, V. Balitskiy, V. Zahorodna, O. Gogotsi and Y. Gogotsi, *Adv. Energy Mater.*, 2020, **22**, 1901241.
18 Y. Li, X. Chen, Y. Sun, X. Meng, Y. Dall'Agnese, G. Chen, C. Dall'Agnese, H. Ren, S. Sasaki, H. Tamiaki and X. F. Wang, *Adv. Mater. Interfaces*, 2020, **7**, 1902080.
19 T. S. Mathis, K. Maleski, A. Goad, A. Sarycheva, M. Anayee, A. C. Foucher, K. Hantanasirisakul, C. E. Shuck, E. A. Stach and Y. Gogotsi, *ACS Nano*, 2021, **15**, 6420–6429.
20 X. Han, L. An, Y. Hu, Y. Li, C. Hou, H. Wang and Q. Zhang, *Appl. Catal., B*, 2020, **265**, 118539.
21 R. Xiao, C. Zhao, Z. Zou, Z. Chen, L. Tian, H. Xu, H. Tang, Q. Liu, Z. Lin and X. Yang, *Appl. Catal., B*, 2020, **268**, 118382.

 This journal is © The Royal Society of Chemistry 2022

Published on 19 1401. Downloaded on 08/11/1404 05:47:49 ..

22 F. He, B. Zhu, B. Cheng, J. Yu, W. Ho and W. Macyk, *Appl. Catal., B*, 2020, **272**, 119006.
23 X. Xie and N. Zhang, *Adv. Funct. Mater.*, 2020, **30**, 2002528.
24 J. Ran, G. Gao, F. T. Li, T. Y. Ma, A. Du and S. Z. Qiao, *Nat. Commun.*, 2017, **8**, 13907.
25 Y. Yang, Z. Zeng, G. Zeng, D. Huang, R. Xiao, C. Zhang, C. Zhou, W. Xiong, W. Wang, M. Cheng, W. Xue, H. Guo, X. Tang and D. He, *Appl. Catal., B*, 2019, **258**, 117956.
26 S. Cao, B. Shen, T. Tong, J. Fu and J. Yu, *Adv. Funct. Mater.*, 2018, **28**, 1800136.
27 J. Xuan, Z. Wang, Y. Chen, D. Liang, L. Cheng, X. Yang, Z. Liu, R. Ma, T. Sasaki and F. Geng, *Angew. Chem.*, 2016, **128**, 14789–14794.
28 X. Wu, J. Wang, Z. Wang, F. Sun, Y. Liu, K. Wu, X. Meng and J. Qiu, *Angew. Chem., Int. Ed.*, 2021, **60**, 9416–9420.
29 H. Xu, A. Ren, J. Wu and Z. Wang, *Adv. Funct. Mater.*, 2020, **30**, 2000907.
30 J. Xuan, Z. Wang, Y. Chen, D. Liang, L. Cheng, X. Yang, Z. Liu, R. Ma, T. Sasaki and F. Geng, *Angew. Chem.*, 2016, **128**, 14789–14794.
31 A. Miranda, J. Halim, M. W. Barsoum and A. Lorke, *Appl. Phys. Lett.*, 2016, **108**, 33102.
32 R. Li, L. Zhang, L. Shi and P. Wang, *ACS Nano*, 2017, **11**, 3752–3759.
33 X. Fan, Y. Ding, Y. Liu, J. Liang and Y. Chen, *ACS Nano*, 2019, **13**, 8124–8134.
34 K. Chaudhuri, M. Alhabeb, Z. Wang, V. M. Shalaev, Y. Gogotsi and A. Boltasseva, *ACS Photonics*, 2018, **5**, 1115–1122.
35 H. Lin, X. Wang, L. Yu, Y. Chen and J. Shi, *Nano Lett.*, 2017, **17**, 384–391.
36 D. B. Velusamy, J. K. El Demellawi, A. M. El Zohry, A. Giugni, S. Lopatin, M. N. Hedhili, A. E. Mansour, E. Di Fabrizio, O. F. Mohammed and H. N. Alshareef, *Adv. Mater.*, 2019, **31**, 1807658.
37 N. Zhang, C. Han, X. Fu and Y. J. Xu, *Chem*, 2018, **4**, 1832–1861.
38 S. Linic, P. Christopher and D. B. Ingram, *Nat. Mater.*, 2011, **10**, 911–921.
39 S. Peng, J. M. McMahon, G. C. Schatz, S. K. Gray and Y. Sun, *Proc. Natl. Acad. Sci. U. S. A.*, 2010, **107**, 14530–14534.
40 J. K. El Demellawi, S. Lopatin, J. Yin, O. F. Mohammed and H. N. Alshareef, *ACS Nano*, 2018, **12**, 8485–8493.
41 D. Magne, V. Mauchamp, S. Célérier, P. Chartier and T. Cabioc'h, *Phys. Rev. B: Condens. Matter Mater. Phys.*, 2015, **91**, 201409.
42 V. Mauchamp, M. Bugnet, E. P. Bellido, G. A. Botton, P. Moreau, D. Magne, M. Naguib, T. Cabioc'h and M. W. Barsoum, *Phys. Rev. B: Condens. Matter Mater. Phys.*, 2014, **89**, 235428.
43 X. Wang, C. Garnero, G. Rochard, D. Magne, S. Morisset, S. Hurand, P. Chartier, J. Rousseau, T. Cabioc'h, C. Coutanceau, V. Mauchamp and S. Célérier, *J. Mater. Chem. A*, 2017, **5**, 22012–22023.
44 X. Yu, X. Jin, X. Chen, A. Wang, J. Zhang, J. Zhang, Z. Zhao, M. Gao, L. Razzari and H. Liu, *ACS Nano*, 2020, **14**, 13876–13885.
45 Q. Ruan, X. Ma, Y. Li, J. Wu, Z. Wang, Y. Geng, W. Wang, H. Lin and L. Wang, *Nanoscale*, 2020, **12**, 20522–20535.
46 W. Yuan, L. Cheng, Y. An, S. Lv, H. Wu, X. Fan, Y. Zhang, X. Guo and J. Tang, *Adv. Sci.*, 2018, **5**, 1700870.
47 J. Low, B. Dai, T. Tong, C. Jiang and J. Yu, *Adv. Mater.*, 2019, **31**, 1807920.
48 Y. Li, X. Deng, J. Tian, Z. Liang and H. Cui, *Appl. Mater. Today*, 2018, **13**, 217–227.
49 Z. Zhang, A. Li, S. W. Cao, M. Bosman, S. Li and C. Xue, *Nanoscale*, 2014, **6**, 5217–5222.
50 L. Yuan, B. Weng, J. C. Colmenares, Y. Sun and Y.-J. Xu, *Small*, 2017, **13**, 1702253.
51 N. Zhang, S. Xie, B. Weng and Y. J. Xu, *J. Mater. Chem. A*, 2016, **4**, 18804–18814.
52 C. Yu, X. Xie and N. Zhang, *Catal. Sci. Technol.*, 2021, **11**, 425–443.
53 Z. Jiang, K. Qian, C. Zhu, H. Sun, W. Wan, J. Xie, H. Li, P. K. Wong and S. Yuan, *Appl. Catal., B*, 2017, **210**, 194–204.
54 V. N. Rao, N. L. Reddy, M. M. Kumari, P. Ravi, M. Sathish, K. M. Kuruvilla, V. Preethi, K. R. Reddy, N. P. Shetti, T. M. Aminabhavi and M. V. Shankar, *Appl. Catal., B*, 2019, **254**, 174–185.
55 J. Wu, Y. Huang, W. Ye and Y. Li, *Adv. Sci.*, 2017, **4**, 1700194.
56 J. Y. Li, Y. H. Li, F. Zhang, Z. R. Tang and Y. J. Xu, *Appl. Catal., B*, 2020, **269**, 118783.
57 Y. C. Chen, Y. K. Hsu, R. Popescu, D. Gerthsen, Y. G. Lin and C. Feldmann, *Nat. Commun.*, 2018, **9**, 232.
58 R. R. Ishiki, H. M. Ishiki and K. Takashima, *Chemosphere*, 2005, **58**, 1461–1469.
59 M. C. Ceballos-Chuc, C. M. Ramos-Castillo, J. J. Alvarado Gil, G. Oskam and G. Rodríguez-Gattorno, *J. Phys. Chem. C*, 2018, **122**, 19921–19930.
60 M. L. Lin, M. Miscuglio, A. Polovitsyn, Y. C. Leng, B. Martín-García, I. Moreels, P. H. Tan and R. Krahne, *J. Phys. Chem. Lett.*, 2019, **10**, 399–405.
61 G. Yu, J. Qian, P. Zhang, B. Zhang, W. Zhang, W. Yan and G. Liu, *Nat. Commun.*, 2019, **10**, 1–8.
62 E. Cortés, P. G. Etchegoin, E. C. Le-Ru, A. Fainstein, M. E. Vela and R. C. Salvarezza, *J. Am. Chem. Soc.*, 2013, **135**, 2809–2815.
63 W. X. Wang, S. H. Liang, T. Yu, D. H. Li, Y. B. Li and X. F. Han, *J. Appl. Phys.*, 2011, **109**, 07C501.
64 Z. Mao, W. Song, X. Xue, W. Ji, L. Chen, J. R. Lombardi and B. Zhao, *J. Phys. Chem. C*, 2012, **116**, 26908–26918.
65 Z. Li, Y. Yan, S. Xu, H. Zhou, M. Xu, L. Ma, M. Shao, X. Kong, B. Wang, L. Zheng and H. Duan, *Nat. Commun.*, 2022, **13**, 147.
66 A. Miranda, J. Halim, A. Lorke and M. W. Barsoum, *Mater. Res. Lett.*, 2017, **5**, 322–328.
67 C. Zhan, Y. Xu, L. Bu, H. Zhu, Y. Feng, T. Yang, Y. Zhang, Z. Yang, B. Huang, Q. Shao and X. Huang, *Nat. Commun.*, 2021, **12**, 6261.